Published in final edited form as:
MAGMA. 2016 April ; 29(2): 259–276. doi:10.1007/s10334-015-0498-z.

Segmentation and quantification of adipose tissue by magnetic resonance imaging

Houchun Harry Hu[1], **Jun Chen**[2], and **Wei Shen**[3]

[1]Department of Radiology, Phoenix Children's Hospital, 1919 East Thomas Road, Phoenix, AZ 85016, USA

[2]Obesity Research Center, Department of Medicine, Columbia University Medical Center, 1150 Saint Nicholas Avenue, New York, NY 10032, USA

[3]Obesity Research Center, Department of Medicine and Institute of Human Nutrition, Columbia University Medical Center, 1150 Saint Nicholas Avenue, New York, NY 10032, USA

Abstract

In this brief review, introductory concepts in animal and human adipose tissue segmentation using proton magnetic resonance imaging (MRI) and computed tomography are summarized in the context of obesity research. Adipose tissue segmentation and quantification using spin relaxation-based (e.g., T1-weighted, T2-weighted), relaxometry-based (e.g., T1-, T2-, T2*-mapping), chemical-shift selective, and chemical-shift encoded water–fat MRI pulse sequences are briefly discussed. The continuing interest to classify subcutaneous and visceral adipose tissue depots into smaller sub-depot compartments is mentioned. The use of a single slice, a stack of slices across a limited anatomical region, or a whole body protocol is considered. Common image post-processing steps and emerging atlas-based automated segmentation techniques are noted. Finally, the article identifies some directions of future research, including a discussion on the growing topic of brown adipose tissue and related segmentation considerations.

Keywords

Adipose tissue; Body composition; Computed tomography; Magnetic resonance imaging; Obesity; Quantification; Segmentation

Introduction and background

This review seeks to provide introductory concepts on the topic of human adipose tissue (AT) segmentation and quantification using magnetic resonance imaging (MRI) and computed tomography (CT) data. Adipose tissue is one of the largest compartments in the human body. The need for accurate, precise, and reliable tools to segment and quantify AT distribution throughout the body using non-invasive imaging data has become increasingly

---

Correspondence to: Houchun Harry Hu.

Compliance with ethical standards
Conflict of interest
The authors declare that they have no conflict of interest.

important in recent years. The demand for clinically relevant measurements of AT quantities is driven by the rising worldwide prevalence of obesity [1, 2] and associated metabolic abnormalities, such as diabetes and liver diseases. There is ubiquitous evidence that excessive accumulation of AT, especially visceral AT (VAT) and ectopic organ fat, are detrimental to one's health and increases one's risk of cardiovascular and metabolic diseases [3–5].

Quantitative measures are useful in research studies to assess cross-sectional [6–8] AT distribution differences between age, gender [9, 10], ethnicity [11, 12], and pathological conditions [13]. In longitudinal studies, temporal measurements can be used to determine the efficacies of interventions such as bariatric surgery [14], diet restrictions [15, 16], weight loss programs, and physical exercise regimens [17], aimed at reducing AT, or conversely, in studies to examine how AT patterns evolve throughout the lifespan, in fetuses [18], in infants and children [19–23], and in adults [24, 25]. The ability to determine AT distribution within the body, for example, as the volume ratio of subcutaneous AT (SAT) to VAT [26, 27], is informative in stratifying those who are obese, but metabolically normal versus those who are of normal weight, but are metabolically "at risk" [28, 29]. Finally, the need to correlate AT quantities with vital signs, hormone and enzyme levels, and cardiac function for ease of data comprehension in population studies has led to the concept of imaging-omics, or Imiomics [30], where whole body imaging data is integrated with non-imaging biomarkers to generate quantitative statistical representations (i.e., correlation maps) of morphological and biological characteristics within a cohort.

In biology, the term fat typically denotes fatty acids and triglyceride molecules, and more generally, lipids [31]. Although the term fat is often used synonymously with AT in the tissue segmentation literature, it is important to realize that fat and AT measurements from various modalities reflect two slightly different, but nonetheless correlated quantities. Fat is the dominant component of white AT (WAT). WAT also consists of an appreciable amount of proteins, minerals, and water [32]. In vivo, while a large proportion of total body fat is found in WAT, significant amounts of fat can also be found outside of WAT, in organs, circulating blood, and cellular organelles (see Fig. 1 from Ref. [31]). Traditional body composition methods such as anthropometric measurements, air-displacement plethysmography (ADP), bioelectric impedance (BIA), dual energy X-ray absorptiometry (DXA), and quantitative magnetic resonance (QMR) estimate total body or regional fat mass, not specifically AT quantities [33]. In comparison to MRI and CT, the operation of these modalities does not usually involve labor and time-intensive post-processing segmentation steps. In their output fat measurements, the minority components of proteins, minerals, and water in AT are excluded. However, fat outside of AT, such as in organs and muscles, are typically included as well.

This review focuses on the segmentation and quantification of WAT from 2D and 3D magnetic resonance imaging (MRI) data and 2D computed tomography (CT). MRI and CT [34] are the only modalities that can provide multidimensional visualizations of the anatomy and delineate SAT and VAT depots. In recent years, however, emerging DXA algorithms for estimating VAT have also been reported [35]. With these AT volume and mass measurements, both the majority fat component and the minority components of proteins, minerals, and water within AT are typically included. However, fat outside of AT can be regionally excluded, by post-processing segmentation. Despite the subtle difference in definition between fat and AT, there is ample evidence in the literature to suggest that AT volume and mass measurements from MRI and CT data correlate with traditional total-body and regional fat mass measurements from BIA, ADP, DXA, and QMR (Table 1, see Refs. [36–45]).

The review is divided into five subsequent parts. First, the generation of lean versus AT signal contrast in CT and MRI is summarized in the "Adipose tissue signal contrast in CT and MRI" section. Strong signal contrast differentiating AT from other anatomical structures is a key prerequisite step to successful segmentation. Next, "Commonly quantified human adipose tissue depots" section highlights common AT compartments that are quantified and reported in the literature. The "Single-slice, regional multi-slice, and whole body acquisitions" section discusses the use of a single slice measurement, a stack of multiple slices across a limited region (i.e., abdomen), or a whole body (i.e., head-to-feet) imaging exam for data acquisition. The "Common segmentation steps" section provides a narrative of some common post-processing steps employed in manual, semiautomated (or supervised), and automated AT segmentation algorithms. Many of these concepts share commonality with similar tools used in brain tissue segmentation, and the reader is referred to an earlier reference for useful details [46]. Finally, the "Conclusion and future directions" section concludes with some directions of future research, including a discussion on brown AT (BAT). Through this introductory review, the authors aim to familiarize the reader with basic concepts and nomenclature in current CT- and MRI-based AT segmentation and quantification methods.

Adipose tissue signal contrast in CT and MRI

AT depots can be identified and differentiated from other anatomical structures on transverse CT images using the data's intrinsic signal intensities, expressed in the Hounsfield Unit (HU), a measure of tissue X-ray attenuation. On a calibrated CT system, pure water has a HU density of zero. With the exception of air in the background, in lungs, and in gastrointestinal tracts, AT is the only other structure in vivo that is represented by a range of negative HU density values [47, 48], while all other non-adipose-tissue structures occupy the positive HU range. In the literature, slightly different negative HU ranges have been used to threshold WAT with similar outcomes, such as −190 to −30 [49, 50], −190 to −45 [51], −150 to −50 [10, 52], −130 to −10 [53], and −250 to −50 [54]. These reported differences in HU range are likely a consequence of variations in system calibrations, differences in the protocol used to acquire the CT data, such as X-ray dosage settings and slice thickness, and potentially reflect minor physiological differences, such as fatty acid composition, in AT between the studied cohorts. Figure 1 illustrates two CT slices. A simple threshold of the data, for example, between the −190 and −30 HU, can generally yield a reasonable initial estimate of total AT across the slice.

The value of MRI in assessing AT distribution within the human body has been established for several decades [55–57]. Similarly, the utility of semi-automated and automated segmentation algorithms to quantify AT in animal models has been established (Table 2, see

Refs. [58–67]), and many of the developed algorithmic steps have been translated to human applications [68, 69]. Unlike CT, MRI provides a variety of pulse sequences, including T1- and T2-weighted imaging, chemical (frequency)-selective imaging (e.g., water suppression), and chemical-shift encoded imaging, to generate signal contrast between adipose and non-adipose tissue. A technical description is beyond the scope of this review, and the reader is referred to recent reviews for further methodological details [7, 70].

However, regardless of the particular type of pulse sequence that is employed, the typical common endpoint of these MRI techniques is to generate a data set where AT is significantly brighter, or hyperintense, in contrast to non-adipose tissue structures [71]. Like CT, the acquisition of transverse slices remains a popular approach. In contrast to CT and the relatively consistent HU representation, signal intensities in typical MR images have no defined units. The range of values representing AT also varies from scanner to scanner, is dependent on the specific pulse sequence used to acquire the data, is influenced by hardware such as radiofrequency transmit gain, radiofrequency receive coils, and can differ from subject to subject. Consequently, unlike CT, no common threshold range exists in MRI to extract adipose tissue.

Another typical feature in MR images that can challenge tissue segmentation is spatially varying signal intensity non-uniformity, which leads to inhomogeneous tissue signal contrast. This undesirable effect is caused by two major sources, the non-uniform B1− magnetic field related to the use of multi-element radiofrequency coil arrays employed for signal reception, and secondly the B1+ magnetic field, which relates to local non-uniformities in the spatial distribution of the flip angle map (i.e., the radiofrequency transmit field) employed in a pulse sequence for spin excitation. At 3 T and higher main magnetic field strengths, B1+ and B1− field inhomogeneities can be exacerbated by susceptibility and dielectric effect, particularly in the abdomen and pelvis regions [72].

Multi-channel radiofrequency transmit technology has been introduced in recent years to mitigate the effects of B1+ inhomogeneities [73]. Although multi-element receive coil arrays are beneficial in enhancing signal-to-noise ratio, they impart noticeable signal variability over the image, with anatomies closer to the receiver elements exhibiting brighter signal intensities than tissues located farther away. Thus, internal AT often appears darker than SAT, and the latter can exhibit signal intensity hot spots at the periphery of the anatomy. These observed inhomogeneities in signal intensity and tissue contrast, often referred to as the bias field, are spatially smooth and slowly varying. Bias field correction aimed at minimizing non-physiological inhomogeneous tissue signal intensity has been extensively studied in the literature [74–78] and is an increasingly used, if not requisite, post-processing step prior to AT segmentation and quantification [79]. Table 3 (see Refs. [80–90]) summarizes some recent literature references on bias field correction, and Fig. 2 illustrates several exemplary images.

An emerging alternative to the aforementioned signal intensity variability in MRI is the use of a proton-density fat fraction map [91] from multi-echo chemical-shift encoded water–fat MRI for AT segmentation. As the name implies, the fat fraction map is consistently normalized to a scale of 0–100 %, and fat-dominant WAT typically occupies a high fat fraction range from 70 to 90 % [92]. By taking the ratio of two separated image data sets—water and fat—the proton-density fat fraction map effectively cancels the aforementioned bias field effect. One recent approach proposed by Poonawalla et al. [93] was to use a lower-bound fat fraction threshold of $\eta_{\max}/2$, where $\eta_{\max}$ is a subject-specific true maximum fat fraction of AT measured in a homogeneous region-of-interest within SAT. This approach yields a reasonable estimate of a preliminary total AT binary mask, as shown in Fig. 3. Figure 4 additionally illustrates an example of proton-density fat fraction map and chemical-shift encoded water–fat MRI in a dog.

With chemical-shift encoded water–fat imaging using gradient-echo pulse sequences, several additional output images spatially co-registered to the fat fraction map are available and can be used to assist AT segmentation. One parameter is the T2* map. Although T2* values are primarily used to quantify organ iron overload in the liver, heart, and pancreas [94], they can be exploited to further delineate WAT from adjacent muscles, and to remove unwanted voxels from bowel and bone marrow. Co-registered in-phase (water + fat) images are also available, and can be used to remove spurious background noise and air in gastrointestinal tracts. Opposed-phase (water–fat) images can be used to identify boundaries and detect relevant edges at the interface of adipose and non-adipose tissues.

In addition to T2* mapping, spin-echo and hybrid gradient- and spin-echo based water–fat pulse sequences can be used to estimate T2 relaxation [95]. Pandey et al. [96] has recently demonstrated the combined use of fat fraction and T2 maps for segmenting parenchyma and blood vessels within the liver. T2 mapping has also been used to assess fat deposition in lower extremity skeletal muscles [97] by taking advantage of the fact that the T2 relaxation rate of fat is distinctively longer than that of lean muscles.

While T1-weighted and fat-selective methods have been widely used and remain popular, the increasing commercial availability of chemical-shift encoded water–fat pulse sequences and fat fraction maps has led to its greater adoption in recent years. All of these techniques are equally capable of providing suitable data for segmentation and quantification of AT depots. Alabousi et al. [98], recently compared T1-weighted protocols against chemical-shift encoded MRI and demonstrated that the latter can be less sensitive to partial volume effects and false-positive errors in quantifying VAT.

Commonly quantified human adipose tissue depots

The segmentation and quantification of SAT and VAT depots spanning the chest and thorax, abdominal, and pelvic anatomies by CT and MRI represent the majority of literature reports, as there is clear evidence that the build-up of adipocytes and the accumulation of fat in these compartments are strong determinants of one’s metabolic health. SAT resides between the dermis and the aponeuroses and fasciae of the muscles. It is a well-defined compartment with clear boundaries that can be visualized and segmented. Recent efforts have been made to split the SAT depot into superficial (sSAT) and deep (dSAT) compartments [99], which are separated by a thin fascial plane. There is also growing evidence that the dSAT compartment is more strongly correlated with metabolic abnormalities [100]. As the fascial plane is not always visible on imaging data [101], anterior and posterior abdominal SAT have been used as approximates of sSAT and dSAT compartments [102], via a line dissecting the abdomen using the anterior edge of the vertebrae as a landmark [103].

Although the VAT depot consists of multiple sub-compartments, including intrathoracic, intra-abdominal, and intrapelvic AT, VAT in the literature is used to represent broadly the sum of one or more of these sub-compartments. The primary reason for this generalization is because the sub-compartments are anatomically connected, with the exception of intrathoracic, epicardial, and pericardial AT depots [104–108]. Unlike the clear boundary differentiation between SAT and VAT depots, a similarly clear delineation of anatomical borders between VAT sub-compartments in CT and MRI by semi-automated and automated segmentation algorithms is difficult, if not impossible. Retroperitoneal and intraperitoneal (e.g., omental, mesenteric) AT depots are also often reported collectively as part of VAT. Specifically, omental and mesenteric AT are likely related to obesity and metabolic health risks since the two depots drain through the portal vein. In specific studies where these depots are quantified, manual segmentation by an experienced user with strong knowledge of anatomy is and remains the preferred approach [109–112]. Supraphrenic AT is typically excluded from VAT estimates. Finally, abdominal intermuscular AT (IMAT), paraosseal AT, and paravertebral AT depots along the body trunk are also commonly included in VAT quantification, and are rarely quantified as separate entities. In metabolic studies, however, IMAT in the lower extremities is typically quantified as a separate depot. Studies have shown IMAT as a significant contributor to metabolic disorders, independent of VAT [113–115]. In the extremities, AT is commonly separated by SAT and perimuscular AT depots. The latter can be further differentiated between intermuscular and intramuscular compartments [116–119]. Lastly, bone marrow AT is typically not segmented unless it is a specific endpoint to a particular study [120]. Bone marrow AT also responds differently to caloric restriction compared to SAT, VAT, and IMAT, and may play a role in osteoporosis [121–123].

Single-slice, regional multi-slice, and whole body acquisitions

Data acquisition protocols for AT quantification vary from the use of a single-slice [124], a stack of slices (2D multi-slice or 3D volume acquisition) across a limited anatomical region (typically the abdomen) [125], or a whole body (head-to-feet) approach [37, 126]. Protocols centered at and about the L2-L3 and L4-L5 lumbar intervertebral spaces, as well as at the umbilicus, are the most popular choices for single and multi-slice protocols in CT and MRI. Because of ionizing radiation exposure concerns, whole body protocols are rarely used in CT studies. In recent years, methodological advancements in hardware and data acquisition speed have led to the availability of whole body 3D volumetric MRI with contiguous slices [127], offering minimal to moderate increases in total scan time in comparison to traditional single and multi-slice approaches. However, single-slice and regional multi-slices remain attractive in large-scale studies, as the effort to post-process and segment these smaller data sets via manual and semiautomated approaches can be significantly shorter than 3D contiguous whole body volumes. Single- and multi-slice approaches are suitable for cross-sectional comparisons between subjects, while multi-slice and whole body are more appropriate in longitudinal studies to track AT changes within an individual [17]. It has been shown that a single-slice measurement of SAT and VAT is a poor predictor of adiposity changes during weight loss [128].

Several studies have demonstrated that a single-slice cross-sectional area measurement of SAT taken at 5 cm below the L4-L5 vertebral disk or near the L3-L4 landmark was the strongest correlate with whole body SAT [129, 130], and that a single-slice measurement predictor for abdominal VAT was best quantified at 5–10 cm above L4–L5, at T12–L1, or at the L1–L2 level [131, 132]. Kuk et al. [133] has shown with data from 85 men that the association between metabolic syndrome parameters and a single-slice cross-sectional area measurement of SAT is nearly independent of the measurement location between the T10 and S1 vertebrae. For VAT, however, the investigators reported significant variations in the association strength with metabolic syndrome parameters, with the strongest correlation observed at the measurement site of the L1–L2 vertebrae. Similar findings were reported by Kuk et al. [134] in a follow-up study in postmenopausal women. Consensus towards a set of standardized protocols and anatomical location for AT measurements remains challenging, as it is likely dependent on the study cohort’s body mass index (BMI), age, gender, ethnicity, and various other anthropometric characteristics. The topic continues to be debated [135, 136]. Furthermore, there also exist notable variations in the slice thickness reported in literature, as well as the inter-slice gap in 2D acquisitions. Findings from a few examples are summarized below.

Thomas et al. [137] reported in a cohort of 54 female participants (BMI range 19–40 kg/m^2) and 13 female subjects with Prader–Willi syndrome (BMI range 23.6–51.6 kg/m^2) the use of a whole body MRI protocol involving 10-mm slices and demonstrated an increase in the coefficient of variation of 1.16 %/cm in the standard error of the mean estimate of AT content when the interslice gap was varied from 0 to 6 cm. This increase was similar for estimates of SAT, VAT, and total body AT. The investigators concluded that a 3-cm inter-slice gap was a reasonable operating point and balanced tradeoffs between quantitative accuracy, requisite scan time, and the total data post-processing time for their study. Shen et al. [138] concluded through an extensive MRI study of 73 children that an interslice gap of 5 cm in a whole body protocol is adequate for estimating SAT in both group and individual-based comparisons. A 5-cm gap was almost as accurate as a contiguous 3D data set for SAT and skeletal muscle quantification. For comparing differences in VAT and IMAT, a smaller interslice gap of 3 cm was recommended.

Schwenzer et al. [139] reported in a cohort of 367 adult volunteers at risk of type 2 diabetes encompassing a BMI range of 19–47 kg/m^2 that area measurements of SAT and VAT made across a single 10 mm slice at the level of the umbilicus correlated strongly with total body AT volume in both males and females, where total body AT was determined from a whole body MRI data set acquired with 10-mm slices and 10-mm interslice gaps. Measurements of total AT area at the level of the head of the humerus and at the head of the femur yielded similarly strong correlations with total body AT volumes. Schaudinn et al. [125] recently evaluated the predictive accuracy of single and multi-slice MRI in the estimation of abdominopelvic VAT volume in 197 overweight and obese patients (BMI range 25–39 kg/m^2) using a 10-mm slice thickness and a small 0.5-mm interslice gap, nearly-contiguous protocol. Single-slice area measurements were made at the level of each of the following landmarks: intervertebral spaces at L1 through L5 and at S1, umbilicus, and femoral head. A volume measurement consisting of a stack of five slices was also made, centered at these locations. The strongest correlations with total abdominopelvic VAT were found for single- and 5-slice measurements at L3–L4 in women and L2–L3 in men. These findings reinforce previous results by Maislin et al. [140].

Common segmentation steps

Manual, semi-automated, and automated AT segmentations procedures typically share a common set of core image processing steps [141]. These steps are briefly summarized below. It is beyond the scope of this review to describe each step in detail, and the reader is referred to the image processing literature for details. Table 4 (see Refs. [92, 142–161]) provides representative citations from recent literature on the automated segmentation of SAT, VAT, and muscle AT depots, using a combination of these post-processing steps. As with manual and supervised segmentation approaches, rigorous training of the analysts on anatomy and proper usage of these post-processing tools remain paramount to ensure consistent and reliable results. Furthermore, the successful performance of many of the segmentation algorithms summarized in Table 4 fundamentally depends on imaging features of WAT that are statistically different than other tissues and structures in vivo.

Signal intensity-based histogram thresholding relies on the ability of the user or algorithm to select easily a threshold from a bi- or multi-modal histogram that either completely or partially separates AT from other anatomical structures. With CT data, histograms are based on Hounsfield Units. With MRI data, the histograms can be based on either the measured raw signal intensity, a quantitative relaxometry parameter such as in T1, T2, or T2* maps, or a quantitative index such as the proton-density fat fraction. Otsu’s method of threshold selection is frequently employed [162, 163], and the overall process is typically accompanied by the generation of a binary mask that aims to remove irrelevant voxels from the data, such as air in the imaging background and in gastrointestinal tracts. The thresholding step is often preceded by a bias field correction algorithm. Fuzzy C-means and K-means clustering algorithms are then employed in conjunction with histogram thresholding to classify voxels into coarse tissue categories such as air, bone, muscle, and adipose tissue.

Edge detection steps, including watershed methods, graph cut algorithms, level set approaches, and active contour snakes (i.e., energy minimizing splines) are often incorporated into the binary mask generation process, to determine the outer boundaries of the body (i.e., the dermis), the interface between SAT depots and internal body structures (i.e., aponeuroses and fasciae of the muscles), as well as internal boundaries between AT depots, organs, and the skeleton. Morphological operations (e.g., dilation, erosion, opening, and closing) can be used to refine the binary mask further. A conversion from spatial Cartesian coordinates to polar coordinates can facilitate edge detection procedures.

Region growing procedures are ubiquitously found in segmentation algorithm pipelines. A single initial seed voxel or multiple seed voxels within AT are identified first. Next, neighboring voxels with signal intensities that fall within a specified set of criteria (e.g., absolute range, percent difference) and spatial constraints (e.g., extent of connectedness with adjacent voxels) are then automatically labeled and added to the growing region-of-interest. Region growing is a particularly effective technique at automatically classifying large patches of AT, such as the SAT and VAT depots. Finally, geometric models are often employed to remove areas around the spine, in order to exclude vertebral bone marrow adipose tissue. Commercial software packages are available for semi-automated AT segmentation [164]. Software that includes useful plug-ins for tissue segmentation are Osirix, ImageJ, 3D Slicer, Matlab, Analyze, and ITK-SNAP.

An emerging approach to segment automatically whole body data sets is based on the concept of building a pre-defined manually segmented “ground truth” atlas dictionary that serves as a reasonable representation of the population at-large [165]. Atlas-based segmentation is a well-established concept that has been widely applied to brain structures [166–168]. Its application to adipose tissue segmentation is a logical extension, and the paradigm is schematically illustrated in Fig. 5. A target data set to be segmented is first registered to a comparable data set from the atlas dictionary. The chosen atlas can be selected based on anthropometric data. Once the non-rigid registration and resultant deformation field is computed between the target and atlas, the deformation is applied to the previously manually segmented tissue classification labels from the chosen atlas. The deformed labels, which correspond to the target data set, represent the automated segmentation results and can be subsequently quantified. The procedure can be iterative, and multiple atlas candidates from the dictionary can be sequentially chosen and selected to refine the non-rigid registration process.

Conclusion and future directions

Through this review, the authors have attempted to provide the reader with sufficient introductory materials and literature references on the topic of human adipose tissue segmentation. In conclusion, robust AT segmentation and quantification has become an integral component in body composition and obesity research. In the past, post-processing and manual image segmentation has long been recognized as a time-consuming and daunting task, particularly in longitudinal studies involving hundreds of subjects, each potentially with tens to hundreds of imaging slices. While many innovative semi-automated and automated segmentation algorithms have been proposed and continue to emerge in the literature, one challenge is that many of these algorithms are not easily accessible to obesity and body composition investigators at large, who may not necessarily be experts in imaging. The scientific community should promote wider availability of AT segmentation algorithms, and strategies should be developed to enable standardization and harmonization of imaging protocols, post-processing algorithms, data pipelines, and analyst training across the field, such that results from different research groups can be more easily compared.

While AT segmentation approaches have been predominantly based on using the tissue’s signal intensity, several investigators have considered the use of multi-parametric MRI data. In addition to the use of the aforementioned fat fraction metric from chemical-shift encoded water–fat MRI, recent reports have proposed utilizing MR relaxometry in AT to facilitate segmentation. Using a dual flip angle approach, Kullberg et al. created whole body T1 maps and demonstrated superior histogram separation of lean and AT voxels based on T1 values rather than the traditional signal intensity approach [169]. T1 mapping of AT appears advantageous, as fat is characterized by one of the shortest T1 values in vivo. In another report by Garnov et al., the investigators discovered the T1 of SAT to be significantly shorter than that of VAT, in both obese subjects and lean controls. Additionally, obese subjects showed statistically significant T1 differences between their sSAT and dSAT compartments [170]. Similarly, Gensanne et al. [171] have investigated the T2 relaxation properties of AT. Furthermore, it has been well established that the degree of triglyceride unsaturation differs between sSAT and dSAT, VAT, and ectopic organ fat [172, 173]. Multi-parametric mapping of AT can thus provide complementary information in addition to image signal intensity, and should be exploited in future studies to improve the robustness, reliability, and speed of segmentation and quantification. In addition to AT segmentation, many of the developed algorithms have been successfully translated to other tissue compartments, in particular in skeletal muscles [174–176]. Further extension towards automated segmentation of bone marrow AT and possibly organs for ectopic fat quantification should be investigated, as the latter is already solidly established with CT data [177, 178].

As an extension of atlas-based automated segmentation, techniques that can automatically segment AT and organs from a subject’s MRI data at subsequent time points while using a priori information from the same subject’s baseline segmentations will be highly attractive. Conceptually, the atlas-based segmentation paradigm can be applied not only to different individuals, but also, and perhaps more easily, to the same individual enrolled in a longitudinal study. In other words, the target and the atlas can be the same person, at different time points, with limited changes in body composition. The capability of achieving rapid intra-subject 3D registration, segmentation, and quantification will provide investigators with detailed person-specific information reflecting the temporal change in fat distribution and volumes in response to intervention. Such capability will also exploit the richness of 3D whole body MRI.

Finally, the non-invasive imaging of human brown AT (BAT) with positron emission and computed tomography (PET/CT), MRI, and combined PET/MR modalities has become widely popular in recent years [179], motivated by increasing evidence of BAT’s role and physiological relevance to human metabolism, energy regulation, and obesity [180]. With PET/CT, voxels containing metabolically active BAT are identified by their appearance on PET images with standard uptake values (SUV) above a minimum threshold, and on co-registered CT images that exhibit “adipose tissue-like” negative HU values. In MRI and PET/MR, fat fraction maps from chemical-shift encoded water–fat MRI have been used to identify BAT in lieu of CT HU, as BAT contains a lower fat fraction than triglyceride-rich WAT.

While semi-automated and automated algorithms for segmenting metabolically active human BAT have been proposed with co-localized PET/CT data, predominantly within the supraclavicular and cervical regions, similar work using data from standalone MRI and PET/MR has only started to emerge in the literature and additional development and validations are needed [181]. The segmentation of human BAT is challenging, even in manual and semi-automated form. In contrast to well-defined SAT and VAT depots, human

BAT is notably present in scattered distributions within the body, and often exists in small cell clusters of arbitrary shape, surrounded by WAT, muscle, and bone where boundary delineation is difficult, if not impossible [182]. The development of robust algorithms for quantifying both metabolically active and inactive (i.e., metabolically quiescent) human BAT volume remains highly desirable, particularly in short-term serial studies aimed at assessing the transition or change from inactive to active BAT quantities in subjects that undergo cold-temperature or pharmacological stimulations, and in extended longitudinal studies investigating the tissue's involvement in human growth [183].

Acknowledgments

H. Hu acknowledges research support from Philips Healthcare and literature reference assistance from librarian Kathy Zeblisky, MLS, of Phoenix Children's Hospital.

References

1. Wang Y, Lobstein T. Worldwide trends in childhood overweight and obesity. Int J Ped Obes. 2006; 1:11–25.
2. Flegal KM, Carroll MD, Ogden CL, Curtin LR. Prevalence and trends in obesity among US adults, 1999–2008. JAMA. 2010; 303:235–241. [PubMed: 20071471]
3. Després JP, Lemieux I, Bergeron J, et al. Abdominal obesity and the metabolic syndrome: contribution to global cardio-metabolic risk. Arterioscler Thromb Vasc Biol. 2008; 28:1039–1049. [PubMed: 18356555]
4. Matsuzawa Y, Funahashi T, Nakamura T. The concept of metabolic syndrome: contribution of visceral fat accumulation and its molecular mechanism. J Atheroscler Thromb. 2011; 18:629–639. [PubMed: 21737960]
5. Bizino MB, Sala ML, de Heer P, et al. MR of multi-organ involvement in the metabolic syndrome. Magn Reson Imaging Clin N Am. 2015; 23:41–58. [PubMed: 25476673]
6. Silver HJ, Welch EB, Avison MJ, Niswender KD. Imaging body composition in obesity and weight loss: challenges and opportunities. Diabetes Metab Syndr Obes. 2010; 28:337–347.
7. Machann J, Horstmann A, Born M, Hesse S, Hirsch FW. Diagnostic imaging in obesity. Best Pract Res Clin Endocrinol Metab. 2013; 27:261–277. [PubMed: 23731887]
8. MacDonald AJ, Greig CA, Baracos V. The advantages and limitations of cross-sectional body composition analysis. Curr Opin Support Palliat Care. 2011; 5:342–349. [PubMed: 21986910]
9. Lemieux S, Prud'homme D, Bouchard C, Tremblay A, Després JP. Sex differences in the relation of visceral adipose tissue accumulation to total body fatness. Am J Clin Nutr. 1993; 58:463–467. [PubMed: 8379501]
10. Conway JM, Yanovski SZ, Avila NA, Hubbard VS. Visceral adipose tissue differences in black and white women. Am J Clin Nutr. 1995; 61:765–771. [PubMed: 7702017]
11. Kadowaki T, Sekikawa A, Murata K, et al. Japanese men have larger areas of visceral adipose tissue than Caucasian men in the same levels of waist circumference in a population-based study. Int J Obes (Lond). 2006; 30:1163–1165. [PubMed: 16446744]
12. Koska J, Stefan N, Votruba SB, Smith SR, Krakoff J, Bunt JC. Distribution of subcutaneous fat predicts insulin action in obesity in sex-specific manner. Obesity (Silver Spring). 2008; 16:2003–2009. [PubMed: 18551127]
13. Engelson ES, Kotler DP, Tan Y, et al. Fat distribution in HIV-infected patients reporting trances enlargement quantified by whole-body magnetic resonance imaging. Am J Clin Nutr. 1999; 69:1162–1169. [PubMed: 10357734]
14. Klein S, Fontana L, Young VL, et al. Absence of an effect of liposuction on insulin action and risk factors for coronary heart disease. N Engl J Med. 2004; 350:2549–2557. [PubMed: 15201411]

15. Mayer LE, Klein DA, Black E, et al. Adipose tissue distribution after weight restoration and weight maintenance in women with anorexia nervosa. Am J Clin Nutr. 2009; 90:1132–1137. [PubMed: 19793856]
16. Cordes C, Dieckmeyer M, Ott B, et al. MR-detected changes in liver fat, abdominal fat, and vertebral bone marrow fat after a four-week calorie restriction in obese women. J Magn Reson Imaging. 2015; doi: 10.1002/jmri.24908
17. Machann J, Thamer C, Stefan N, et al. Follow-up whole-body assessment of adipose tissue compartments during a lifestyle intervention in a large cohort at increased risk for type 2 diabetes. Radiology. 2010; 257:353–363. [PubMed: 20713612]
18. Anblagan D, Deshpande R, Jones NW, et al. Measurement of fetal fat in utero in normal and diabetic pregnancies using magnetic resonance imaging. Ultrasound Obstet Gynecol. 2013; 42:335–340. [PubMed: 23288811]
19. Kabir N, Forsum E. Estimation of total body fat and subcutaneous adipose tissue in full-term infants less than 3 months old. Pediatr Res. 1993; 34:448–454. [PubMed: 8255676]
20. Harrington TA, Thomas EL, Frost G, Modi N, Bell JD. Distribution of adipose tissue in the newborn. Pediatr Res. 2004; 55:437–441. [PubMed: 14681496]
21. Brambilla P, Bedogni G, Moreno LA, et al. Crossvalidation of anthropometry against magnetic resonance imaging for the assessment of visceral and subcutaneous adipose tissue in children. Int J Obes (Lond). 2006; 30:23–30. [PubMed: 16344845]
22. Fields DA, Teague AM, Short KR, Chernausek SD. Evaluation of DXA vs. MRI for body composition measures in 1-month olds. Pediatr Obes. 2015; doi: 10.1111/ijpo.12021
23. Lange T, Beuchert M, Baumstark MW, et al. Value of MRI and MRS fat measurements to complement conventional screening methods for childhood obesity. J Magn Reson Imaging. 2015; doi: 10.1002/jmri.24919
24. Siegel MJ, Hildebolt CF, Bae KT, Hong C, White NH. Total and intraabdomianl fat distribution in preadolescents and adolescents: measurement with MR imaging. Radiology. 2007; 242:846–856. [PubMed: 17244720]
25. Khoo CM, Leow MK, Sadananthan SA, et al. Body fat partitioning does not explain the interethnic variation in insulin sensitivity among Asian ethnicity: the Singapore adult metabolism study. Diabetes. 2014; 63:1093–1102. [PubMed: 24353181]
26. Stefan N, Kantartzis K, Machann J, et al. Identification and characterization of metabolically benign obesity in humans. Arch Intern Med. 2008; 168:1609–1616. [PubMed: 18695074]
27. Thomas EL, Parkinson JR, Frost GS, et al. The missing risk: MRI and MRS phenotyping of abdominal adiposity and ectopic fat. Obesity (Silver Spring). 2012; 20:76–87. [PubMed: 21660078]
28. St-Onge MP, Janssen I, Heymsfield SB. Metabolic syndrome in normal-weight Americans: new definition of the metabolically obese, normal-weight individual. Diabetes Care. 2004; 27:2222–2228. [PubMed: 15333488]
29. Kelishadi R, Cook SR, Motlagh ME, et al. Metabolically obese normal weight and phenotypically obese metabolically normal youths: the CASPIAN study. J Am Diet Assoc. 2008; 108:82–90. [PubMed: 18155992]
30. Kullberg, J.; Johansson, L.; Lind, L.; Ahlström, H.; Strand, R. Imiomics: bringing -omics to whole body imaging: examples in cross-sectional interaction between whole-body MRI and non-imaging data. Proceedings of the 23rd scientific meeting, International Society for Magnetic Resonance in Medicine; Toronto. 2015. p. 3757
31. Shen W, Wang Z, Punyanitya M, et al. Adipose tissue quantification by imaging methods: a proposed classification. Obes Res. 2003; 11:5–16. [PubMed: 12529479]
32. Thomas LW. The chemical composition of adipose tissue of man and mice. Q J Exp Physiol Cogn Med Sci. 1962; 47:179–188. [PubMed: 13920823]
33. Lee YS, Gallagher D. Assessment methods in human body composition. Curr Opin Clin Nutr Metab Care. 2008; 11:566–572. [PubMed: 18685451]
34. Thomas EL, Fitzpatrick JA, Malik SJ, Taylor-Robinson SD, Bell JD. Whole body fat: content and distribution. Prog Nucl Magn Reson Spectrosc. 2013; 73:56–80. [PubMed: 23962884]

35. Kaul S, Rothney MP, Peters DM, et al. Dual-energy X-ray absorptiometry for quantification of visceral fat. Obesity (Silver Spring). 2012; 20:1313–1318. [PubMed: 22282048]
36. Mourtzakis M, Prado CM, Lieffers JR, Reiman T, McCargar LJ, Baracos VE. A practical and precise approach to quantification of body composition in cancer patients using computed tomography images acquired during routine care. Appl Physiol Nutr Metab. 2008; 33:997–1006. [PubMed: 18923576]
37. Kullberg J, Brandberg J, Angelhed JE, et al. Whole-body adipose tissue analysis: comparison of MRI, CT, and dual energy X-ray absorptiometry. Br J Radiol. 2009; 82:123–130. [PubMed: 19168691]
38. Bredella MA, Ghomi RH, Thomas BJ, et al. Comparison of DXA and CT in the assessment of body composition in pre-menopausal women with obesity and anorexia nervosa. Obesity (Silver Spring). 2010; 18:2227–2233. [PubMed: 20111013]
39. Metzinger MN, Miramontes B, Zhou P, et al. Correlation of X-ray computed tomography with quantitative nuclear magnetic resonance methods for pre-clinical measurement of adipose and lean tissues in living mice. Sensors (Basel). 2014; 14:18526–18542. [PubMed: 25299952]
40. Varady KA, Santosa S, Jones PJ. Validation of hand-held bioelectrical impedance analysis with magnetic resonance imaging for the assessment of body composition in overweight women. Am J Hum Biol. 2007; 19:429–433. [PubMed: 17421003]
41. Ludescher B, Machann J, Eschweiler GW, et al. Correlation of fat distribution in whole body MRI with generally used anthropometric data. Invest Radiol. 2009; 44:712–719. [PubMed: 19809346]
42. Browning LM, Mugridge O, Dixon AK, Aitken SW, Prentice AM, Jebb SA. Measuring abdominal adipose tissue: comparison of simpler methods with MRI. Obes Facts. 2011; 4:9–15. [PubMed: 21372606]
43. Ludwig UA, Klausmann F, Baumann S, et al. Whole-body MRI-based fat quantification: a comparison to air displacement plethysmography. J Magn Reson Imaging. 2014; 40:1437–1444. [PubMed: 24449401]
44. Karlsson AK, Kullberg J, Stokland E, Allvin K, Gronowitz E, Svensson PA, Dahlgren J. Measurements of total and regional body composition in preschool children: a comparison of MRI, DXA, and anthropometric data. Obesity (Silver Spring). 2013; 21:1018–1024. [PubMed: 23784906]
45. Silver HJ, Niswender KD, Kullberg J, et al. Comparison of gross body fat–water magnetic resonance imaging at 3 Tesla to dual-energy X-ray absorptiometry in obese women. Obesity (Silver Spring). 2013; 21:765–774. [PubMed: 23712980]
46. Clarke LP, Velthuizen RP, Camacho MA, et al. MRI segmentation: methods and applications. Magn Reson Imaging. 1995; 13:343–368. [PubMed: 7791545]
47. Baba S, Jacene HA, Engles JM, Honda H, Wahl RL. CT Hounsfield units of brown adipose tissue increase with activation: preclinical and clinical studies. J Nucl Med. 2010; 51:246–250. [PubMed: 20124047]
48. Ahmadi N, Hajsadeghi F, Conneely M, et al. Active brown and white adipose tissues with computed tomography. Acad Radiol. 2013; 20:1443–1447. [PubMed: 24119358]
49. Kvist H, Chowdhury B, Grangård U, Tylén U, Sjöström L. Total and visceral adipose tissue volumes derived from measurements with computed tomography in adult men and women: predictive equations. Am J Clin Nutr. 1988; 48:1351–1361. [PubMed: 3202084]
50. Yoshizumi T, Nakamura T, Yamane M, et al. Abdominal fat: standardized technique for measurement at CT. Radiology. 1999; 211:283–286. [PubMed: 10189485]
51. Maurovich-Horvat P, Massaro J, Fox CS, Moselewski F, O'Donnell CJ, Hoffmann U. Comparison of anthropometric, area- and volume-based assessment of abdominal subcutaneous and visceral adipose tissue volumes using multi-detector computed tomopgrahy. Int J Obes (Lond). 2006; 31:500–506. [PubMed: 16953256]
52. El-Serag H, Hashmi A, Garcia J, et al. Visceral abdominal obesity measured by CT scan is associated with an increased risk of Barrett's oesophagus: a case–control study. Gut. 2014; 63:220–229. [PubMed: 23408348]

53. Seidell JC, Bakker CJ, van der Kooy K. Imaging techniques for measuring adipose tissue distribution—a comparison between computed tomography and 1.5T magnetic resonance. Am J Clin Nutr. 1990; 51:953–957. [PubMed: 2349931]

54. Enzi G, Biondetti PR, Fiore D, Semisa M, Zurlo F. Subcutaneous and visceral fat distribution according to sex, age, and overweight, evaluated by computed tomopgrahy. Am J Clin Nutr. 1986; 44:739–746. [PubMed: 3788827]

55. Sobol W, Rossner S, Hinson B, et al. Evaluation of a new magnetic resonance imaging method for quntitating adipose tissue areas. Int J Obes (Lond). 1991; 15:589–599.

56. Fowler PA, Fuller MF, Glasbey CA, et al. Total and subcutaneous adipose tissue in women: the measurement of distribution and accurate prediction of quantity by using magnetic resonance imaging. Am J Clin Nutr. 1991; 54:18–25. [PubMed: 2058582]

57. Shen W, Liu H, Punyanitya M, Chen J, Heymsfield SB. Pediatric obesity phenotyping by magnetic resonance imaging. Curr Opin Clin Nutr Metab Care. 2005; 8:595–601. [PubMed: 16205458]

58. Fowler PA, Fuller MF, Glasbey CA, Cameron CG, Foster MA. Validation of in vivo measurement of adipose tissue by magnetic resonance imaging of lean and obese pig. Am J Clin Nutr. 1992; 56:7–13. [PubMed: 1609764]

59. Mitchell AD, Scholz AM, Wange PC, Song H. Body composition analysis of the pig by magnetic resonance imaging. J Anim Sci. 2001; 79:1800–1813. [PubMed: 11465367]

60. Ranefall P, Bidar AW, Hockings PD. Automatic segmentation of intra-abdominal and subcutaneous adipose tissue in 3D whole mouse MRI. J Magn Reson Imaging. 2009; 30:554–560. [PubMed: 19711401]

61. Luu YK, Lublinsky S, Ozcivici E, Capilla E, Pessin JE, Rubin CT, Judex S. In vivo quantification of subcutaneous and visceral adiposity by micro-computed tomography in a small animal model. Med Eng Phys. 2009; 31:34–41. [PubMed: 18486521]

62. Johnson DH, Flask CA, Ernsberger PR, Wong WC, Wilson DL. Reproducible MRI measurement of adipose tissue volumes in genetic and dietary rodent obesity models. J Magn Reson Imaging. 2008; 28:915–927. [PubMed: 18821617]

63. Johnson DH, Narayan S, Wilson DL, Flask CA. Body composition analysis of obesity and hepatic steatosis in mice by relaxation compensated fat fraction (RCFF) MRI. J Magn Reson Imaging. 2012; 35:837–843. [PubMed: 22095745]

64. Tang Y, Sharma P, Nelson MD, Simerly R, Moats RA. Automatic abdominal fat assessment in obese mice using a segmented shape model. J Magn Reson Imaging. 2011; 34:866–873. [PubMed: 21769982]

65. Sasser TA, Chapman SE, Li S, et al. Segmentation and measurement of fat volumes in murine obesity models using X-ray computed tomography. J Vis Exp. 2012; doi: 10.3791/3680

66. Garteiser P, Doblas S, Towner RA, Griffin TM. Calibration of a semi-automated segmentation method for quantification of adipose tissue compartments from magnetic resonance images of mice. Metabolism. 2013; 62:1686–1695. [PubMed: 23890668]

67. Gifford A, Kullberg J, Berglund J, et al. Canine body composition quantification using 3 Tesla fat–water MRI. J Magn Reson Imaging. 2014; 39:485–491. [PubMed: 23596090]

68. Monziols M, Collewet G, Mariette F, Kouba M, Davenel A. Muscle and fat quantification in MRI gradient echo images using a partial volume detection method. Application to the characterization of pig belly tissue. Magn Reson Imaging. 2005; 23:745–755. [PubMed: 16198830]

69. Kremer PV, Förster Scholz AM. Use of magnetic resonance imaging to predict the body composition of pigs in vivo. Animal. 2013; 7:879–884. [PubMed: 23228200]

70. Hu HH, Kan HE. Quantitative proton MR techniques for measuring fat. NMR Biomed. 2013; 26:1609–1629. [PubMed: 24123229]

71. Gronemeyer SA, Steen RG, Kauffman WM, Reddick WE, Glass JO. Fast adipose tissue (FAT) assessment by MRI. Magn Reson Imaging. 2000; 18:815–818. [PubMed: 11027874]

72. Schick F. Whole-body MRI at high field: technical limits and clinical potential. Eur Radiol. 2005; 15:946–959. [PubMed: 15856252]

73. Katscher U, Börnert P. Parallel RF transmission in MRI. NMR Biomed. 2006; 19:393–400. [PubMed: 16705630]

74. Axel L, Constantini J, Listerud J. Intensity correction in surface-coil MR imaging. AJR. 1987; 148:418–420. [PubMed: 3492123]

75. Wang D, Doddrell DM. Method for a detailed measurement of image intensity nonuniformity in magnetic resonance imaging. Med Phys. 2005; 32:952–960. [PubMed: 15895578]

76. Chen, W. A fuzzy c-means (FCM) based algorithm for intensity inhomogeneity correction and segmentation of MR images. IEEE international symposium on biomedical imaging: nano to macro; 2004. p. 1307-1310.

77. Lin M, Chan S, Chen JH, et al. A new bias field correction method combining N3 and FCM for improved segmentation of breast density on MRI. Med Phys. 2011; 38:5–14. [PubMed: 21361169]

78. Hou Z. A review of MR image intensity inhomogeneity correction. Int J Biomed Imaging. 2006; doi: 10.1155/IJBI/2006/49151

79. Peterson P, Romu T, Brorson H, Leinhard OD, Månsson S. Fat quantification in skeletal muscle using multigradient-echo imaging: comparison of fat and water references. J Magn Reson Imaging. 2015; doi: 10.1002/jmri.24972

80. Collewet G, Davenel A, Toussaint C, Akoka S. Correction of intensity nonuniformity in spin-echo T1-weighted images. Magn Reson Imaging. 2002; 20:365–373. [PubMed: 12165356]

81. Yang GZ, Myerson S, Chabat F, Pennell DJ, Firmin DN. Automatic MRI adipose tissue mapping using overlapping mosaics. MAGMA. 2002; 14:39–44. [PubMed: 11796251]

82. Kullberg J, Ahlström H, Johansson L, Frimmel H. Automated and reproducible segmentation of visceral and subcutaneous adipose tissue from abdominal MRI. Int J Obes (Lond). 2007; 31:1806–1817. [PubMed: 17593903]

83. Positano V, Cusi K, Santarelli MF, et al. Automatic correction of intensity inhomogeneities improves unsupervised assessment of abdominal fat by MRI. J Magn Reson Imaging. 2008; 28:403–410. [PubMed: 18666138]

84. Leinhard, OD.; Johansson, A.; Rydell, J.; Smedby, O.; Nystrom, F.; Lundberg, P.; Borga, M. Quantitative abdominal fat estimation using MRI. IEEE international conference on pattern recognition; 2008. p. 1-4.

85. Romu, T.; Borga, M.; Leinhard, OD. MANA – Multi scale adaptive normalized averaging. IEEE international symposium on biomedical imaging: nano to macro; 2011. p. 361-364.

86. Andersson T, Romu T, Karlsson A, et al. Consistent intensity inhomogeneity correction in water–fat MRI. J Magn Reson Imaging. 2015; 42:468–476. [PubMed: 25355066]

87. Sussman, DL.; Yao, J.; Summers, RM. Automated fat measurement and segmentation with intensity inhomogeneity correction. Proceedings of SPIE 7623, medical imaging 2010: image processing; 2010. p. 76233X

88. Azzabou, N.; de Sousa, PL.; Carlier, PG. Non-uniformity correction using cosine functions basis and total variation constraint. IEEE international symposium on biomedical imaging: nano to macro; 2010. p. 748-751.

89. Mosbech, TH.; Pilgaard, K.; Vaag, A.; Larsen, R. Automatic segmentation of abdominal adipose tissue in MRI. Image analysis: 17th Scandinavian conference, SCIA, lecture notes in computer science; 2011. p. 501-511.

90. Würslin C, Springer F, Yang B, Schick F. Compensation of RF field and receiver coil induced inhomogeneity effects in abdominal MR images by a priori knowledge of the human adipose tissue distribution. J Magn Reson Imaging. 2011; 34:716–726. [PubMed: 21769975]

91. Reeder SB, Hu HH, Sirlin CB. Proton density fat-fraction: a standardized MR-based biomarker of tissue fat concentration. J Magn Reson Imaging. 2012; 36:1011–1014. [PubMed: 22777847]

92. Addeman BT, Kutty S, Perkins TG, et al. Validation of volumetric and single-slice MRI adipose analysis using a novel fully automated segmentation method. J Magn Reson Imaging. 2014; 41:233–241. [PubMed: 24431195]

93. Poonawalla AH, Sjoberg BP, Rehm JL, et al. Adipose tissue MRI for quantitative measurement of central obesity. J Magn Reson Imaging. 2013; 37:707–716. [PubMed: 23055365]

94. Hernando D, Levin YS, Sirlin CB, Reeder SB. Quantification of liver iron with MRI: state of the art and remaining challenges. J Magn Reson Imaging. 2014; 40:1003–1021. [PubMed: 24585403]

95. Li Z, Graff C, Gmitro AF, Squire SW, Bilgin A, Outwater EK, Altbach MI. Rapid water and lipid imaging with T2 mapping using a radial IDEAL-GRASE technique. Magn Reson Med. 2009; 61:1415–1424. [PubMed: 19353651]
96. Pandey, A.; Bilgin, A.; Cumar, S.; Kalb, B.; Martin, DR.; Altbach, MI. Automated segmentation of liver parenchyma and blood vessel with in vivo radial Gradient and Spin-Echo (GRASE) datasets for characterization of diffuse liver disease. Proceedings of the 21st scientific meeting, International Society for Magnetic Resonance in Medicine; Salt Lake City. 2013. p. 1528
97. Kan HE, Scheenen TW, Wohlgemuth M, Klomp DW, van Loosbroek-Wagenmans I, Padberg GW, Heerschap A. Quantitative MR imaging of individual muscle involvement in facioscapulohumeral muscular dystrophy. Neuromuscul Disord. 2009; 9:357–362.
98. Alabousi A, Al-Attar S, Joy TR, Hegele RA, McKenzie CA. Evaluation of adipose tissue volume quantification with IDEAL fat–water separation. J Magn Reson Imaging. 2011; 34:474–479. [PubMed: 21780238]
99. Walker GE, Verti B, Marzullo P, et al. Deep subcutaneous adipose tissue: a distinct abdominal adipose depot. Obesity (Silver Spring). 2007; 15:1933–1943. [PubMed: 17712110]
100. Lundbom J, Hakkarainen A, Lundbom N, Taskinen MR. Deep subcutaneous adipose tissue is more saturated than superficial subcutaneous adipose tissue. Int J Obes (Lond). 2013; 37:620–622. [PubMed: 22641063]
101. Kelley DE, Thaete FL, Troost F, Huwe T, Goodpaster BH. Subdivisions of subcutaneous abdominal adipose tissue and insulin resistance. Am J Physiol Endocrinol Metab. 2000; 278:E941–E948. [PubMed: 10780952]
102. Misra A, Garg A, Abate N, Peshock RM, Stray-Gundersen J, Grundy SM. Relationship of anterior and posterior subcutaneous abdominal fat to insulin sensitivity in nondiabetic men. Obes Res. 1997; 5:93–99. [PubMed: 9112243]
103. Ross R, Aru J, Freeman J, Hudson R, Janssen I. Abdominal adiposity and insulin resistance in obese men. Am J Physiol Endocrinol Metab. 2002; 282:E657–E663. [PubMed: 11832370]
104. Nichols JH, Samy B, Nasir K, et al. Volumetric measurement of pericardial adipose tissue from contrast-enhanced coronary computed tomography angiography: a reproducibility study. J Cardiovasc Comput Tomogr. 2008; 2:288–295. [PubMed: 19083964]
105. Shahzad R, Bos D, Metz C, et al. Automatic quantification of epicardial fat volume on non-enhanced cardiac CT scans using a multi-atlas segmentation approach. Med Phys. 2013; 40:09190.
106. Elming MB, Lønborg J, Rasmussen T, et al. Measurement of pericardial adipose tissue using contrast enhanced cardiac multidetector computed tomography—comparison with cardiac magnetic resonance imaging. Int J Cardiovasc Imaging. 2013; 29:1401–1407. [PubMed: 23702948]
107. Mihl C, Loeffen D, Versteylen MO, et al. Automated quantification of epicardial adipose tissue (EAT) in coronary CT angiopgraphy: comparison with manual assessment and correlation with coronary artery disease. J Cardiovasc Comput Tomogr. 2014; 8:215–221. [PubMed: 24939070]
108. Spearman JV, Meinel FG, Schoepf UJ, et al. Automated quantification of epicardial adipose tissue using CT angiography: evaluation of a prototype software. Eur Radiol. 2014; 24:519–526. [PubMed: 24192980]
109. Kortelainen ML, Särkioja T. Visceral fat and coronary pathology in male adolescents. Int J Obes Relat Metab Disord. 2001; 25:228–232. [PubMed: 11410824]
110. Liu KH, Chan YL, Chan WB, Chan JC, Chu CW. Mesenteric fat thickness is an independent determinant of metabolic syndrome and identifies subjects with increased carotid intima-media thickness. Diabetes Care. 2006; 29:379–384. [PubMed: 16443891]
111. Bergman RN, Kim SP, Hsu I, et al. Abdominal obesity: role in the pathophysiology of metabolic disease and cardiovascular risk. Am J Med. 2007; 120(2 Suppl 1):S3–S8.
112. Fabbrini E, Tamboli RA, Magkos F, et al. Surgical removal of omental fat does not improve insulin sensitivity and cardiovascular risk factors in obese adults. Gastroenterology. 2010; 139:448–455. [PubMed: 20457158]
113. Albu JB, Kovera AJ, Allen L, et al. Independent association of insulin resistance with larger amounts of intermuscular adipose tissue and a greater actue insulin response to glucose in

African American than in white nondiabetic women. Am J Clin Nutr. 2005; 82:1210–1217. [PubMed: 16332653]

114. Yim JE, Heshka S, Albu J, et al. Intermuscular adipose tissue rivals visceral adipose tissue in independent associations with cardiovascular risk. Int J Obes (Lond). 2007; 31:1400–1405. [PubMed: 17452994]
115. Boettcher M, Machann J, Stefan N, et al. Intermuscular adipose tissue: association with other adipose tissue compartments and insulin sensitivity. J Magn Reson Imaging. 2009; 29:1340–1345. [PubMed: 19422021]
116. Al-Attar SA, Pollex RL, Robinson JF, et al. Semi-automated segmentation and quantification of adipose tissue in calf and thigh by MRI: a preliminary study in patients with mono-genic metabolic syndrome. BMC Med Imaging. 2006; 31:6–11.
117. Karampinos DC, Baum T, Nardo L, et al. Characterization of the regional distribution of skeletal muscle adipose tissue in type 2 diabetes using chemical shift-based water/fat separation. J Magn Reson Imaging. 2012; 35:899–907. [PubMed: 22127958]
118. Mattei JP, Fur YL, Cuge N, Guis S, Cozzone PJ, Bendahan D. Segmentation of fascias, fat and muscle from magnetic resonance images in humans: the DISPIMAG software. MAGMA. 2006; 19:275–279. [PubMed: 17004065]
119. Orgiu S, Lafortuna CL, Rastelli F, Cadioli M, Falini A, Rizzo G. Automatic muscle and fat segmentation in the thigh from T1-weighted MRI. J Magn Reson Imaging. 2015; doi: 10.1002/jmri.25031
120. Casazza K, Hanks LJ, Hildalgo B, Hu HH, Affuso O. Short-term physical activity intervention decreases femoral bone marrow adipose tissue in young children: a pilot study. Bone. 2012; 50:23–27. [PubMed: 21939791]
121. Bathija A, Davis S, Trubowitz S. Bone marrow adipose tissue: response to acute starvation. Am J Hematol. 1979; 6:191–198. [PubMed: 484542]
122. Schwartz AV, Sigurdsson S, Hue TF, et al. Vertebral bone marrow fat associated with lower trabecular BMD and prevalent vertebral fracture in older adults. J Clin Endocrinol Metab. 2013; 98:2294–2300. [PubMed: 23553860]
123. Karampinos DC, Melkus G, Baum T, Bauer JS, Rummeny EJ, Krug R. Bone marrow fat quantification in the presence of trabecular bone: initial comparison between water–fat imaging and single-voxel MRS. Magn Reson Med. 2014; 71:1158–1165. [PubMed: 23657998]
124. Demerath EW, Shen W, Lee M, et al. Approximation of total visceral adipose tissue with a single magnetic resonance image. Am J Clin Nutr. 2007; 85:362–368. [PubMed: 17284730]
125. Schaudinn A, Linder N, Garnov N, et al. Predictive accuracy of single- and multi-slice MRI for the estimation of total visceral adipose tissue in overweight to severely obese patients. NMR Biomed. 2015; 28:583–590. [PubMed: 25808071]
126. Machann J, Thamer C, Schnoedt B, et al. Standardized assessment of whole body adipose tissue topography by MRI. J Magn Reson Imaging. 2005; 21:455–462. [PubMed: 15778954]
127. Börnert P, Keupp J, Eggers H, Aldefeld B. Whole-body 3D water/fat resolved continuously moving table imaging. J Magn Reson Imaging. 2007; 25:660–665. [PubMed: 17326078]
128. Shen W, Chen J, Gantz M, Velasquez G, Punyanitya M, Heymsfield SB. A single MRI slice does not accurately predict visceral and subcutaneous adipose tissue changes during weight loss. Obesity (Silver Spring). 2012; 20:2458–2463. [PubMed: 22728693]
129. Shen W, Punyanitya M, Wang Z, et al. Total body skeletal muscle and adipose tissue volumes: estimation from a single abdominal cross-sectional image. J Appl Physiol. 2004; 97:2333–2338. [PubMed: 15310748]
130. Shen W, Punyanitya M, Wang Z, et al. Visceral adipose tissue: relations between single-slice areas and total volume. Am J Clin Nutr. 2004; 80:271–278. [PubMed: 15277145]
131. Shen W, Punyanitya M, Chen J, et al. Visceral adipose tissue: relationships between single slice areas at different locations and obesity-related health. Int J Obes (Lond). 2007; 31:763–769. [PubMed: 17060927]
132. Irlbeck T, Massaro Jm, Bamberg F, O'Donnel CJ, Hoffman U, Fox CS. Association between single-slice measurements of visceral and abdominal subcutaneous adipose tissue with

volumetric measurements: the Framingham Heart Study. Int J Obes (Lond). 2010; 34:781–787. [PubMed: 20065971]

133. Kuk JL, Church TS, Blair SN, Ross R. Does measurement site for visceral and abdominal subcutaneous adipose tissue alter associations with the metabolic syndrome? Diabetes Care. 2006; 29:679–684. [PubMed: 16505526]
134. Kuk JL, Church TS, Blair SN, Ross R. Measurement site and the association between visceral and abdominal subcutaneous adipose tissue with metabolic risk in women. Obesity (Silver Spring). 2010; 18:1336–1340. [PubMed: 19910940]
135. Thomas EL, Bell JD. Influence of undersampling on magnetic resonance imaging measurements of intra-abdominal adipose tissue. Int J Obes Relat Metab Disord. 2003; 27:211–218. [PubMed: 12587001]
136. Springer F, Ehehalt S, Sommer J, et al. Predicting volumes of metabolically important whole-body adipose tissue compartments in overweight and obese adolescents by different MRI approaches and anthropometry. Eur J Radiol. 2012; 81:1488–1494. [PubMed: 21543171]
137. Thomas EL, Saeed N, Hajnal JV, et al. Magnetic resonance imaging of total body fat. J Appl Physiol. 1998; 85:1778–1785. [PubMed: 9804581]
138. Shen W, Chen J, Kwak S, Punyanitya M, Heymsfield SB. Between-slice intervals in quantification of adipose tissue and muscle in children. Int J Pediatr Obesity. 2011; 6:149–156.
139. Schwenzer NF, Machann J, Schraml C, et al. Quantitative analysis of adipose tissue in single transverse slices for estimation of volumes of relevant fat tissue compartments. Invest Radiol. 2010; 45:788–794. [PubMed: 20829704]
140. Maislin G, Ahmed MM, Gooneratne N, et al. Single slice vs. volumetric MR assessment of visceral adipose tissue, reliability and validity among the overweight and obese. Obesity (Silver Spring). 2012; 20:2124–2132. [PubMed: 22395811]
141. Jin Y, Imielinska CZ, Laine AF, Udupa J, Shen W, Heymsfield SB. Segmentation and evaluation of adipose tissue from whole body MRI scans. Medical image computing and computer-assisted intervention—MICCAI 2003 lecture notes in computer science. 2003; 2878:635–642.
142. Zhao B, Colville J, Kalaigian J, Curran S, Jiang L, Kijewski P, Schwartz LH. Automated quantification of body fat distribution on volumetric compute tomography. J Comput Assist Tomogr. 2006; 30:777–783. [PubMed: 16954927]
143. Ohshima S, Yamamoto S, Yamaji T, et al. Development of an automated 3D segmentation program for volume quantification of body fat distribution using CT. Jpn J Radiol Tech. 2008; 64:1177–1181.
144. Makrogiannis S, Caturegli G, Davatzikos C, Ferrucci L. Computer-aided assessment of regional abdominal fat with food residue removal in CT. Acad Radiol. 2013; 20:1413–1421. [PubMed: 24119354]
145. Nemoto M, Yeernuer T, Masutani Y, et al. Development of automatic visceral fat volume calculation software for CT volume data. J Obes. 2014; doi: 10.1155/2014/495084
146. Liou TH, Chan WP, Pan LC, Lin PW, Chou P. Chen CH (2006) Fully automated large-scale assessment of visceral and subcutaneous abdominal adipose tissue by magnetic resonance imaging. Int J Obes (Lond). 2006; 30:844–852. [PubMed: 16418756]
147. Armao D, Guyon JP, Firat Z, Brown MA, Semelka RC. Accurate quantification of visceral adipose tissue (VAT) using water-saturation MRI and computer segmentation: preliminary results. J Magn Reson Imaging. 2006; 23:736–741. [PubMed: 16555257]
148. Kullberg J, Johansson L, Ahlström H, Courivaud F, Koken P, Eggers H, Börnert P. Automated assessment of whole-body adipose tissue depots from continuously moving bed MRI: a feasibility study. J Magn Reson Imaging. 2009; 30:185–193. [PubMed: 19557740]
149. Kullberg J, Karlsson AK, Stokland E, Svensson PA, Dahlgren J. Adipose tissue distribution in children: automated quantification using water and fat MRI. J Magn Reson Imaging. 2010; 32:204–210. [PubMed: 20575078]
150. Nakai R, Azuma T, Kishimoto T, Hirata T, Takizawa O, Hyon SH, Tsutsumi S. Development of a high-precision image-processing automatic measurement system for MRI visceral fat images acquired using a binomial RF-excitation pulse. Magn Reson Imaging. 2010; 28:520–526. [PubMed: 20096526]

151. Würslin C, Machann J, Rempp H, Claussen C, Yang B, Schick F. Topography mapping of whole body adipose tissue using a fully automated and standardized procedure. J Magn Reson Imaging. 2010; 31:430–439. [PubMed: 20099357]
152. Zhou A, Murillo H, Peng Q. Novel segmentation method for abdominal fat quantification by MRI. J Magn Reson Imaging. 2011; 34:852–860. [PubMed: 21769972]
153. Wald D, Teucher B, Dinkel J, et al. Automatic quantification of subcutaneous and visceral adipose tissue from whole-body magnetic resonance images suitable for large cohort studies. J Magn Reson Imaging. 2012; 36:1421–1434. [PubMed: 22911921]
154. Joshi AA, Hu HH, Leahy RM, Goran MI, Nayak KS. Automatic intra-subject registration-based segmentation of abdominal fat from water–fat MRI. J Magn Reson Imaging. 2013; 37:423–430. [PubMed: 23011805]
155. Thörmer G, Bertram HH, Garnov N, et al. Software for automated MRI-based quantification of abdominal fat and preliminary evaluation in morbidly obese patients. J Magn Reson Imaging. 2013; 37:1144–1150. [PubMed: 23124651]
156. Sadananthan SA, Prakash B, Leow MK, et al. Automated segmentation of visceral and subcutaneous (deep and superficial) adipose tissues in normal and overweight men. J Magn Reson Imaging. 2015; 41:924–934. [PubMed: 24803305]
157. Senseney, J.; Hemler, PF.; McAuliffe, MJ. Automated segmentation of computed tomography images. Proceedings of the 26th IEEE international symposium on computer-based medical systems; 2009. p. 1-7.
158. Positano V, Christiansen T, Santarelli MF, Ringgaard S, Landini L, Gastaldelli A. Accurate segmentation of subcutaneous and intermuscular adipose tissue from MR images of the thigh. J Magn Reson Imaging. 2009; 29:677–684. [PubMed: 19243051]
159. Prescott, JW.; Priddy, M.; Best, TM., et al. An automated method to detect interstitial adipose tissue in thigh muscles for patients with osteoarthritis. Conference Proceedings of IEEE Engineering in Medicine and Biology Society; 2009. p. 6360-6363.
160. Makrogiannis S, Serai S, Fishbein KW, Schreiber C, Ferrucci L, Spencer RG. Automated quantification of muscle and fat in the thigh from water-, fat- and nonsuppressed MR images. J Magn Reson Imaging. 2012; 35:1152–1161. [PubMed: 22170747]
161. Valentinitsch A, Karmapinos DC, Alizai H, Subburaj K, Kumar D, Link TM, Majumdar S. Automated unsupervised multi-parametric classification of adipose tissue depots in skeletal muscle. J Magn Reson Imaging. 2013; 37:917–927. [PubMed: 23097409]
162. Otsu N. A threshold selection method from gray-level histograms. IEEE Trans Syst Man Cybern. 1979; 9:62–66.
163. Sezgin M, Bülent S. Survey over image thresholding techniques and quantitative performance evaluation. J Electron Imaging. 2004; 13:146–168.
164. Bonekamp S, Ghosh P, Crawford S. Quantitative comparison and evaluation of software packages for assessment of abdominal adipose tissue distribution by magnetic resonance imaging. Int J Obes (Lond). 2008; 32:100–111. [PubMed: 17700582]
165. Karlsson A, Rosander J, Romu T, et al. Automatic and quantitative assessment of regional muscle volume by multi-atlas segmentation using whole-body water–fat MRI. J Magn Reson Imaging. 2015; 41:1558–1569. [PubMed: 25111561]
166. Heckemann RA, Keihaninejad S, Alijabar P, Rueckert D, Hajnal JV, Hammers A. Improving intersubject image registration using tissue-class information benefits robustness and accuracy of multi-atlas based anatomical segmentation. NeuroImage. 2010; 51:221–227. [PubMed: 20114079]
167. Iglesias JE, Sabuncu MR. Multi-atlas segmentation of biomedical images: a survey. Med Image Anal. 2015; 24:205–219. [PubMed: 26201875]
168. Devi CN, Chandrasekharan A, Sundararaman VK, Alex ZC. Neonatal brain MRI segmentation: a review. Comput Biol Med. 2015; 64:163–178. [PubMed: 26189155]
169. Kullberg J, Angelhed JE, Lönn L, et al. Whole-body T1 mapping improves the definition of adipose tissue: consequences for automated image analysis. J Magn Reson Imaging. 2006; 24:394–401. [PubMed: 16786577]

170. Garnov N, Linder N, Schaudinn A, et al. Comparison of T1 relaxation times in adipose tissue of severly obese patients and healthy lean subjects measured by 1.5T MRI. NMR Biomed. 2014; 27:1123–1128. [PubMed: 25066754]
171. Gensanne D, Josse G, Theunis J, Lagarde JM, Vincensini D. Quantitative magnetic resonance imaging of subcutaneous adipose tissue. Skin Res Technol. 2009; 15:45–50. [PubMed: 19152578]
172. Phinney SD, Stern JS, Burke KE, Tang AB, Miller G, Holman RT. Human subcutaneous adipose tissue shows site-specific differences in fatty acid composition. Am J Clin Nutr. 1994; 60:725–729. [PubMed: 7942579]
173. Machann J, Stefan N, Schabel C, et al. Fraction of unsaturated fatty acids in visceral adipose tissue (VAT) is lower in subjects with high total VAT volume—a combined 1H MRS and volumetric MRI study in male subjects. NMR Biomed. 2013; 26:232–236. [PubMed: 22972698]
174. Brunner G, Nambia V, Yang E, et al. Automatic quantification of muscle volumes in magnetic resonance imaging scans of the lower extremities. Magn Reson Imaging. 2011; 29:1065–1075. [PubMed: 21855242]
175. Commean PK, Tuttle LJ, Hastings MK, Strube MJ, Mueller MJ. Magnetic resonance imaging measurement reproducibility for calf muscle and adipose tissue volume. J Magn Reson Imaging. 2011; 34:1285–1294. [PubMed: 21964677]
176. Thomas MS, Newman D, Leinhard OD, et al. Test-retest reliability of automated whole body and compartmental muscle volume measurements on a wide bore 3T MR system. Eur Radiol. 2014; 24:2279–2291. [PubMed: 24871333]
177. Tong T, Wolz R, Wang Z, et al. Discriminative dictionary learning for abdominal multi-organ segmentation. Med Image Anal. 2015; 23:92–104. [PubMed: 25988490]
178. Xu Z, Burke RP, Lee CP, et al. Efficient multi-atlas abdominal segmentation on clinically acquired CT with SIMPLE context learning. Med Image Anal. 2015; 24:18–27. [PubMed: 26046403]
179. Borga M, Virtanen KA, Romu T, et al. Brown adipose tissue in humans: detection and functional analysis using PET, MRI, and DECT. Methods Enzymol. 2014; 537:141–159. [PubMed: 24480345]
180. Cypess AM, Haft CR, Laughlin MR, Hu HH. Brown fat in humans: consensus points and experimental guidelines. Cell Metab. 2014; 20:408–415. [PubMed: 25185947]
181. Gifford A, Towse TF, Walker RC, Avison MJ, Welch EB. Human brown adipose tissue depots automatically segmented by positron emission tomography/computed tomography and registered magnetic resonance images. J Vis Exp. 2015; doi: 10.3791/52415
182. Lidell ME, Betz MJ, Leinhard OD, et al. Evidence for two types of brown adipose tissue in humans. Nat Med. 2013; 19:631–634. [PubMed: 23603813]
183. Betz MJ, Enerbäck S. Human brown adipose tissue: what we have learned so far. Diabetes. 2015; 64:2352–2360. [PubMed: 26050667]

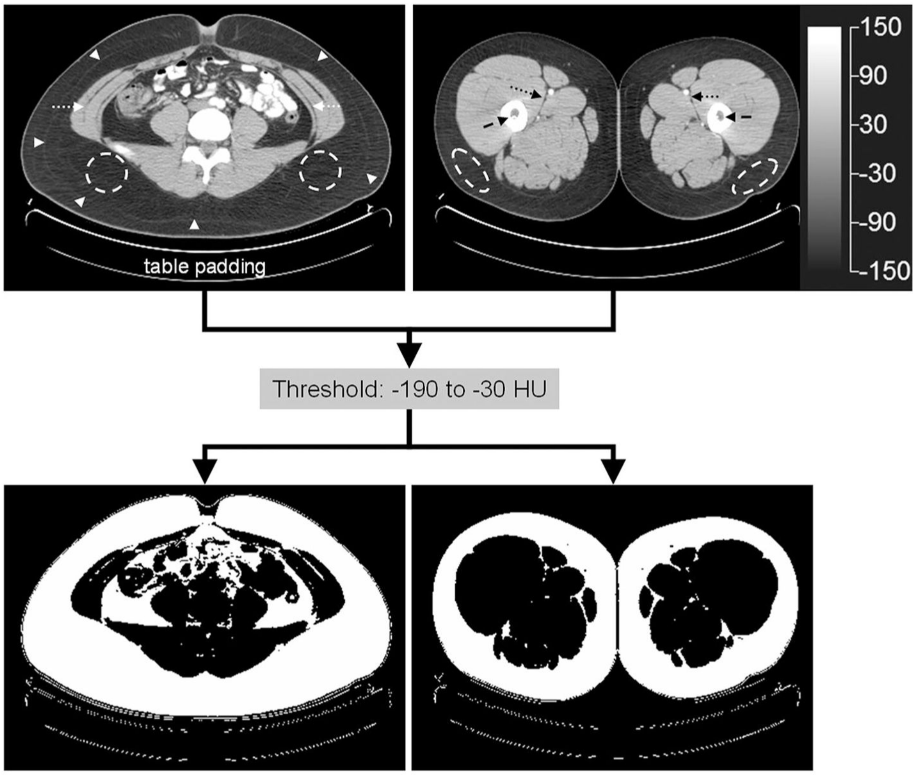

Fig. 1.

Representative axial CT images at the level of the umbilicus (*left*) and the thighs (*right*) from an adult female. The images are displayed on a grayscale range from −150 to 150 X-ray attenuation coefficients, the Hounsfield Unit (HU). In the abdomen, the fascia separating the deep and the superficial subcutaneous adipose tissue layer is visible (*arrowheads*). Because of the high tissue signal contrast between adipose tissue and other compartments such as muscle, fluid, and bone, a simple threshold procedure on the HU values can be used to identify and extract a majority of adipose tissue voxels as a first step towards segmentation. Average HU values in the two abdominal regions of interest (*dashed circles*) are −112 ± 10.9 and −111 ± 12.7 HU. Average values in the thighs (*dashed ovals*) are −104 ± 9.8 and −104 ± 8.1 HU, respectively. Note that some misidentification does occur at edges, in partial volume voxels between adipose and non-adipose tissue layers (i.e., intermuscular adipose tissue, *dotted arrows*), and near hematopoietic red bone marrow (*dashed arrows*). These misidentifications can be remedied or corrected by using a slightly different threshold range or further manual user interaction. Data courtesy of Vicente Gilsanz, Children's Hospital Los Angeles

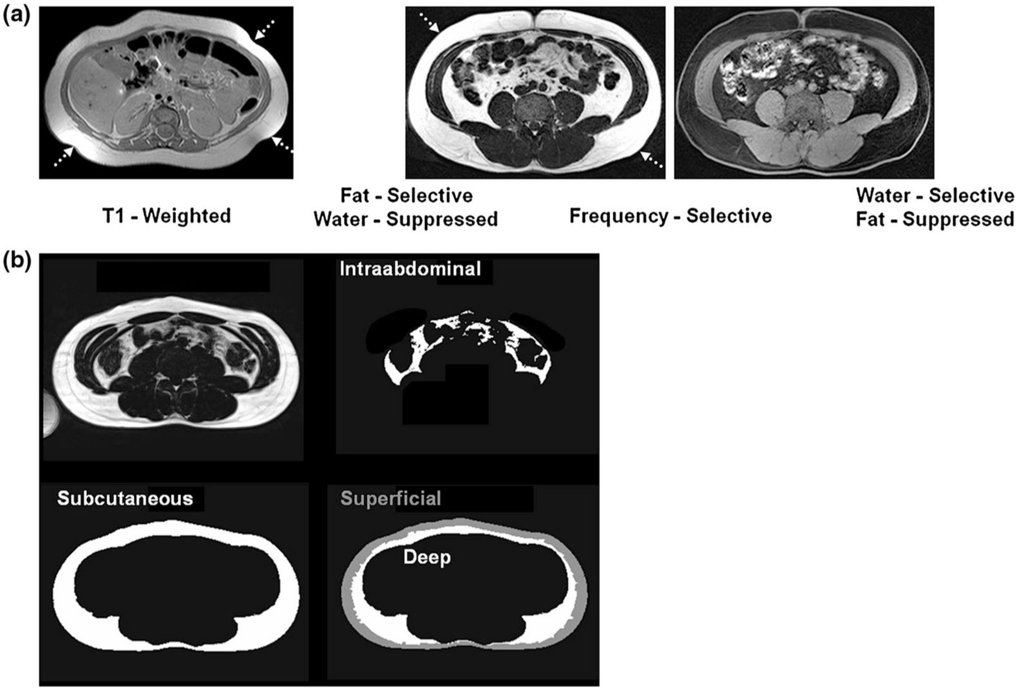

Fig. 2.

Examples of T1-weighted and frequency-selective images from 3 T MRI are shown in the abdomen. For frequency-selective imaging, a corresponding pair of fat-selective and water-selective images is shown in the same subject. Volumetric data are typically acquired using a 2D multi-slice or 3D volume acquisition. Note the strong tissue signal contrast between adipose and lean tissues, a prerequisite in the data that will successfully facilitate subsequent segmentation. *Dotted arrows* in (**a**) denote subcutaneous adipose tissue locations in close proximity to radiofrequency receiver coil elements. These locations exhibit signal intensity variations in comparison to other adipose tissue within the image and is a consequence of the coil array's bias field. **b** illustrates an example of partitioning the subcutaneous adipose tissue further into deep (*white mask*) and superficial (*gray mask*) sub-compartments. Portions of the illustration courtesy of Bryan Addeman, University of Western Ontario, (see Ref. [92] for details) and Sendhil Velan, Singapore Bioimaging Consortium (see Ref. [156] for details)

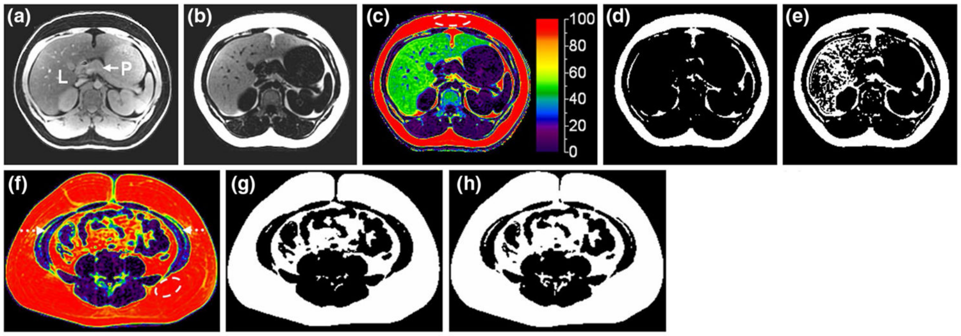

Fig. 3.

a, **b**, **c** Representative MRI axial slices of the abdomen showing the liver (L) and the pancreas (P) in an adult male, acquired with a breath-hold multi (six)-echo chemical-shift encoded water–fat technique at 3 T. Shown are the reconstructed **a** water-only, **b** fat-only, and **c** corresponding proton-density percent fat fraction images, the latter shown on a color scale from 0 to 100 %. The subject has non-alcoholic fatty liver disease (NAFLD), as evidenced by the green color tone of the organ on the percent fat signal (~50 %) image. Note that subcutaneous and intra-abdominal adipose tissues can be clearly seen in *red* (percent fat fraction of 80–100 %), which can facilitate subsequent adipose tissue segmentation. Corresponding binary adipose tissue masks are shown in (**d**) and (**e**), respectively, using a set 70 % lower-bound threshold or a subject-specific $\eta_{max}/2$ % fat signal threshold. η_{max} was determined from the dashed region in (**c**) to be 97 %. Note that in this particular NAFLD subject with a high degree of steatosis, the $\eta_{max}/2$ generated mask in (**e**) can be problematic since voxels within the liver are misidentified as adipose tissue. The percent fat fraction image for a slice at the level of the umbilicus from a different subject is shown in (**f**), along with similar binary masks. η_{max} was measured as 98.3 % within the dashed region in (**f**). Note in (**g**) that partial volume voxels containing intermuscular adipose tissue are mostly missed [*dotted arrows* in (**f**)] when a threshold of 70 % is used. However, they are identified using the $\eta_{max}/2$ threshold in (**h**). Data courtesy of Michael I. Goran and Krishna S. Nayak, University of Southern California

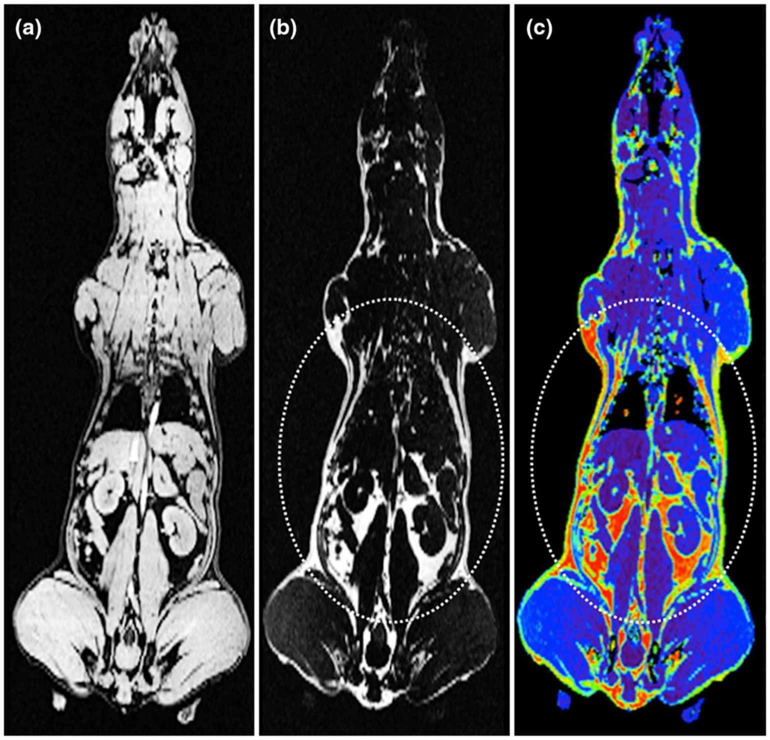

Fig. 4.

Whole body water–fat imaging in a canine, showing **a** separated water, **b** separated fat, and **c** proton-density percent fat fraction map, shown on the same color bar as in Fig. 3c. Adipose tissue in the body trunk region (*dotted circles*) is visually identifiable as hyperin-tense voxels in the fat-only image in (**b**) and by the high percent fat fraction voxels denoted in *red* in (**c**). Data courtesy of Aliya Gifford and E. Brian Welch, Vanderbilt University (see Ref. [67] for details)

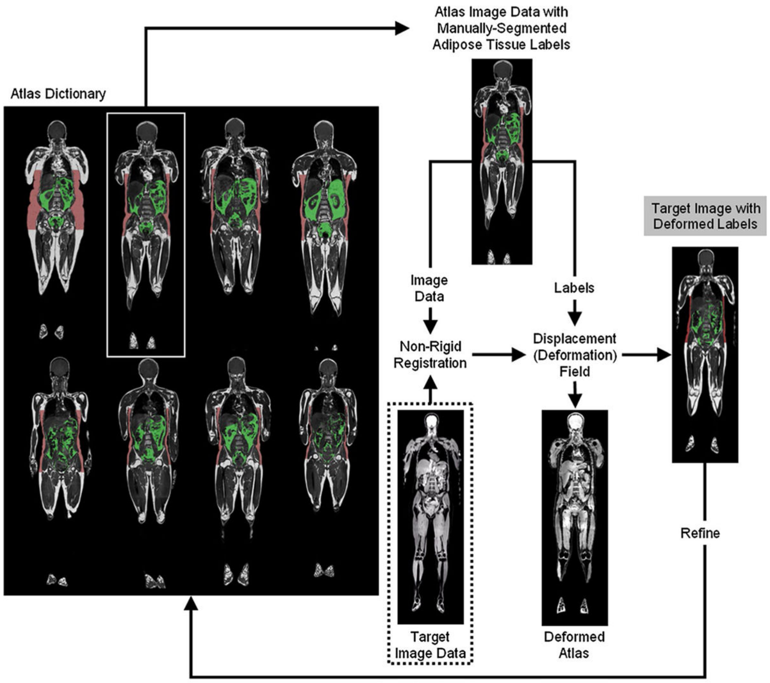

Fig. 5.

A schematic of atlas-based automated segmentation subcutaneous (*red*) and visceral (*green*) of adipose tissues. The target data set to be automatically segmented (*dotted box*) is registered to pre-existing volumes in the atlas, which represents a collection of manually segmented “gold-standard” reference data sets. The non-rigid registration step yields a displacement map, which is then applied to the atlas labels. Multiple atlases can be used to refine the procedure iteratively. In this particular example, the data sets were acquired with chemical-shift encoded water–fat MRI and all data sets have been pre-processed to correct for signal intensity bias field. Note that in this particular case, the water-only image from the target is fed into the non-rigid registration step. Illustration courtesy of Anette Karlsson and Olof Dahlqvist Leinhard, Linköping University (see Ref. [165] for details)

Table 1

Select references from recent literature reporting correlation between CT and MRI-based measurements of adipose tissue versus fat mass obtained by other modalities

	Modality	References	Remarks
CT	BIA	Mourtzakis et al. [36]	DXA and CT superior to BIA, measurements at L3 a strong predictor of whole body values (0.86–0.94 correlations, $p < 0.001$), study in 21 cancer patients
	DXA	Kullberg et al. [37]	Human study in 10 subjects, 0.99 correlation ($p = 0.005$) for whole body adipose tissue analysis between DXA and 28 slices of CT, also included whole body MRI (correlation 0.979, $p = 0.005$ with DXA and 0.995, $p = 0.114$ with CT)
		Bredella et al. [38]	Human study in 39 anorexia nervosa, 34 obese, and 18 lean women, 0.77–0.95 correlations, $p < 0.0001$
	QMR	Metzinger et al. [39]	Semi-automated segmentation, with 0.99 correlation in phantoms, 0.96–0.98 correlations in adipose tissue, mouse study, two groups, $n = 28$ and $n = 17$, p values not reported
MRI	BIA	Varady et al. [40]	BIA underestimated fat mass by 2.3 ± 3.3 kg and percent fat mass by 5.6 ± 3.9 % versus MRI ($p < 0.0001$), study in 31 overweight women
		Ludescher et al. [41]	Human study in 38 volunteers, 17 patients with depression syndrome, and 13 women with bulimia nervosa, 0.72 correlation, $p < 0.0004$, for total body adipose tissue and SAT, 0.096 correlation $p = 0.447$ for VAT, human study
		Browning et al. [42]	Human study, $n = 120$, 20 men and 20 women each in three groups, lean, overweight, and obese, 0.79–0.94 correlations between BIA and MRI total abdominal adipose tissue in men, 0.38–0.74 in women, tested two BIA systems, also included DXA, exact p values not reported, extensive analysis, see reference for details
	ADP	Ludwig et al. [43]	Human study in 11 volunteers, 0.97–0.98 correlations, $p < 0.0001$, for whole body adipose tissue analysis
	DXA	Karlsson et al. [44]	Human study in 105 young children, 0.86–0.88 correlations, $p < 0.001$, between DXA total and trunk fat mass vs. MRI-derived SAT
		Silver et al. [45]	Human study in 12 obese women, 0.98 and 0.80 correlations, $p < 0.0001$, for whole body and total trunk adipose tissue analysis

Table 2

Select recent references, in chronological order, on adipose tissue segmentation and quantification in animal studies

References	Remarks
Fowler et al. [58]	Manual segmentation, lean versus obese pigs, T1-weighted 0.04 T multi-slice MRI, validation with post-mortem carcass chemical analysis
Mitchell et al. [59]	Manual segmentation, pig, T1- and T2-weighted 1.5 and 4.7 T multi-slice MRI, validation with post-mortem carcass chemical analysis
Ranefall et al. [60]	Automated segmentation based on histogram and region-growing schemes, mice, T1- and T2-weighted 9.4 T 3D MRI
Luu et al. [61]	Semi-automated segmentation, mice, microCT, cross-sectional study, in silico validation
Johnson et al. [62]	Semi-automated fat fraction-based segmentation, mice, chemical-shift encoded water–fat 7 T multi-slice MRI, cross-sectional study, in vitro validation
Johnson et al. [63]	
Tang et al. [64]	Automated segmentation based on adaptive fuzzy C-means method, T1-weighted 7 T multi-slice MRI, cross-sectional study
Sasser et al. [65]	Semi-automated segmentation, mice, CT, cross-sectional study
Garteiser et al. [66]	Semi-automated histogram-based segmentation, mice, water-suppressed 7 T multi-slice MRI, cross-sectional study, correlation with DXA
Gifford et al. [67]	Semi-automated fat fraction-based segmentation, dog, chemical-shift encoded water–fat 3 T multi-slice MRI, longitudinal study, correlation with scale weight

Table 3

Select recent references on the correction of signal intensity bias field in MRI data for adipose tissue segmentation and quantification. Additional relevant citations are found therein

References	Remarks
Collewet et al. [80]	Uniform phantom calibration based approach
Yang et al. [81]	Intensity correction algorithm using a linear overlapping mosaic model
Kullberg et al. [82]	Intensity correction algorithm using a polynomial function (i.e., second degree order) to fit a bias field to adipose tissue voxels on a slice-wise basis
Positano et al. [83]	Intensity correction algorithm using adaptive fuzzy C-means clustering
Leinhard et al. [84]	Multi-scale adaptive normalized average (MANA)—intensity correction algorithm exploiting adipose tissue (i.e. pure fat) as an internal intensity reference, typically sparsely sampled, to compute a dense scaling field at each spatial location
Romu et al. [85]	Consistent intensity inhomogeneity correction (CIIC)—MANA in combination with chemical-shift encoded water–fat
Andersson et al. [86]	MRI data to automatically identify pure adipose tissue voxels or pure muscle (water-only) voxels
Sussman et al. [87]	Algorithm using the well-established non-parametric non-uniform intensity normalization (N3) framework
Azzabou et al. [88]	Parametric model based on cosine functions, aimed at reducing the variance in subcutaneous adipose tissue and the total variation of the non-uniformity function. Target application in lower extremities
Mosbech et al. [89]	Intensity correction algorithm using thin plate spine framework to fit a bias field to different classes of tissues
Würslin et al. [90]	Two-step intensity correction algorithm using active contours and thin plate splines to fit sampling points within subcutaneous adipose tissue, followed by additional inclusion of sampling points from visceral adipose tissue

Table 4

Select references from recent literature reporting fully automated approaches in segmenting subcutaneous, visceral, and muscle adipose tissue depots, using CT and MRI data in humans

Compartment	Modality	References	Remarks
Subcutaneous and visceral adipose tissues	CT	Zhao et al. [142]	−190 to −30 HU threshold range, radial profile approach to identify tissue boundaries, compared single-slice measurements at L4 and L5 vertebrae to abdominal volume measurements
		Ohshima et al. [143]	−190 to −30 HU threshold range, radial profile approach to identify abdominal tissue boundaries
		Makrogiannis et al. [144]	FCM to identify air, muscle, fat, and bone tissues, single-slice approach at L4 and L5 vertebrae, separation of subcutaneous and visceral compartments using gradient vector flow, ACM, manual removal of signals from food residues in gastrointenstinal tract
		Nemoto et al. [145]	−190 to −30 HU threshold range, multi-slice approach, data rescaling, removal of air voxels, identification of bone, fat, and muscle voxels, morphological and region-growing operations, validation against manual segmentation, in men and women
	MRI	Liou et al. [146]	T1W and T2W 1.5 T MRI. Four pulse sequences, SI HT, RG, EM, correlation with MA, consideration for motion artifacts and atypical anatomies
		Armao et al. [147]	Multi-slice FS 1.5 T MRI, SI HT, RG, correlation with MA
		Kullberg et al. [148]	3D 1.5 T CSE WFI with continuously moving table, multi- parametric analysis of water-only, fat-only, in-phase (water + fat), water fraction, and fat fraction data, SI HT, MO, lung segmentation, geometric models to exclude bone marrow in spine and pelvis, correlation with MA
		Kullberg et al. [149]	3D 1.5 T CSE WFI, exploits fat fraction data for HT, geometric model to exclude bone marrow and intermuscular adipose tissue, FCM, and MO, correlation with semi-automated analysis, correlation between single-slice and volume measurements, study in children
		Nakai et al. [150]	Multi-slice FS MRI, SI HT, template matching, correlation with MA, short-term longitudinal study
		Würslin et al. [151]	Multi-slice T1W 1.5 T MRI, whole-body analysis, SI HT, FCM, ACM, explicit detection of extremities, correlation with MA
		Zhou et al. [152]	Multi-slice FS 1.5 T MRI, with and without water suppression, SI HT, FCM, ACM and consideration of partial volume effects
		Wald et al. [153]	3D 1.5 T CSE WFI, whole-body analysis, SI HT, statistical shape and appearance models, correlation with MA, large $n = 314$ cohort
		Joshi et al. [154]	3D 3 T CSE WFI, atlas-based approach, correlation with MA
		Thörmer et al. [155]	Multi-slice 1.5 T CSE WFI, FCM, RG, ACM. Correlation with MA in obese cohort
		Addeman et al. [92]	3D 3 T CSE WFI, exploits fat fraction and T2* data, conversion from Cartesian to polar coordinates, surface fitting, correlation with MA, cross-sectional study
		Sadananthan et al. [156]	Multi-slice 3 T CSE WFI, EM, segmentation of superficial and deep subcutaneous depots using graph cut and level set methods, correlation with semi-automated analysis, cross- sectional study
Inter- and intra-muscular adipose tissues	CT	Senseney et al. [157]	Medical Imaging Processing, Analysis, and Visualization (MIPAV) software from the National Institutes of Health (http://mipav.cit.nih.gov/)
	MRI	Positano et al. [158]	Multi-slice T1W 1.5 T MRI, FCM, ACM, SI HT, EM algorithm, correlation with MA
		Prescott et al. [159]	Multi-slice T1W MRI, emphasis on interstitial adipose tissue in OA patients, N3 bias field correction, signal normalization, MO, RG, correlation with MA
		Makrogiannis et al. [160]	3D FS 3 T MRI, multi-parametric approach using water-suppressed and fat-suppressed complementary images, N3 bias field correction, K-means clustering, parametric deformable and ACM, correlation with CT

Compartment	Modality	References	Remarks
		Valentinitsch et al. [161]	3D 3 T CSE WFI, OA and type 2 diabetes cohort, comparison with MA, multi-parametric approach using water-only, fat- only, and in-phase (water + fat) images, K-means clustering, MO, and RG

Additional relevant citations are found therein

ACM active contour models, *CSE WFI* chemical-shift encoded water–fat MRI, *EM* expectation/maximization, *FCM* fuzzy C-means (clustering), *FS* frequency-selective, *HT* histogram thresholding, *MA* manual segmentation analysis, *MO* morphological operations, *OA* osteoarthritis, *RG* region growing, *SI* signal intensity, *T1W/T2W* T1-/T2-weighted